Population Balance Model for Drying of Droplets Containing Aggregating Nanoparticles

Andreas Bück, Mirko Peglow, Martina Naumann, and Evangelos Tsotsas
Chair of Thermal Process Engineering, Otto von Guericke University,
Universitätsplatz 2, 39106 Magdeburg, Germany

DOI 10.1002/aic.13726
Published online January 17, 2012 in Wiley Online Library (wileyonlinelibrary.com).

Drying of droplets containing nanoscaled particles is investigated for the first drying stage by means of a population balance model. The novelty of the model consists in the consideration of not only gas-side heat and mass transfer, and liquid-side diffusion, but also aggregation as a particulate process. Size-dependency of particle mobility links liquid-side mass transport and aggregation, leading to different particle concentration profiles in the droplet depending on the thermal conditions and aggregation kinetics. The main focus of this work lies on the influence of the aggregation kinetics on the profiles, the time of crust formation and the resulting droplet porosity at the end of the first drying stage. Model validation and justification is performed by use of experimental data from literature. © 2012 American Institute of Chemical Engineers
AIChE J, 58: 3318–3328, 2012
Keywords: population balance modeling, droplet drying, spray drying, nanoparticle, aggregation

Introduction

The production of solid particles and powders by spray drying from droplets containing microparticles and nanoparticles is a process widely applied in many industries, for instance in foods, detergents, pharmaceuticals (production of inhalants[1]), and medicine (cancer detection, antibacterial surface coatings).

The growing demands in product quality necessitate a comprehensive understanding of the thermal and solid phase subprocesses, that is, drying and particle formation, during spray drying to produce results that meet high specifications.

According to the droplet morphology, the process can be divided into two stages (Figure 1): in the first drying stage, the droplet enters a hot medium, for instance air. It then obtains sensible heat which leads to evaporation of the liquid and shrinkage of the droplet. The second drying stage starts at the point (the ''locking point'') when the droplet turns into a wet particle, initiating the formation of a dry porous crust at the droplet surface. In this second stage, moisture is still evaporated from the interior of the droplet, but the diameter of the created particle remains constant. However, the drying conditions determine the inner structure of the formed particle which may range from hollow or highly porous to compact.

The heat and mass transfer during drying of liquid droplets is well understood, here numerous theoretical and experimental investigations have been conducted, see for instance Ranz and Marshall[2] and Walton.[3] The solid phase processes (particle formation) on their own are also understood quite well,[4,5] but the coupled process of droplet drying and particle formation is still an open problem.

The coupled process has been addressed in a number of works so far, for instance Charlesworth and Marshall[6] who studied the evaporation from droplets containing dissolved solids; Sano and Keey[7] simulated the particle distribution during drying using mass concentrations. In the work of Nešić and Vodnik[8] a mass balance of the shell is derived, but the main focus lies on the thermal properties (e.g. droplet temperature). Seydel et al.[9] considered the heat and mass transport, and the particle formation by particle growth using population balances for the description of the particles. Mezhericher et al.[10] treat the thermal properties for both drying stages in a distributed way; the solid phase, however, is described by mass concentrations neglecting particle properties. In the works of Handscomb et al.[11,12] heat and mass transfer is considered for both drying stages; they also apply a population balance equation (PBE) to describe the particle formation. As in the work of Seydel et al.[9] they consider particle growth as the dominant particle formation process.

One common observation in these works is that the resulting droplet morphology depends on the thermal conditions and the solid phase properties.

In this contribution, we will extend the work of Seydel et al.[9] and Handscomb et al.[11] by developing a model for the treatment of droplets containing nanoparticles during the first stage of drying that considers the mass and heat transfer of the liquid phase and the particle formation in the dispersed phase. Here, we consider aggregation of nanoparticles as the dominant particle formation process which often has great influence on the product properties, see for instance Gharagozloo and Goodson.[13] To model the solid phase processes a two-dimensional (2-D) population balance[5] is applied.

Correspondence concerning this article should be addressed to A. Bück at Andreas.Bueck@ovgu.de.

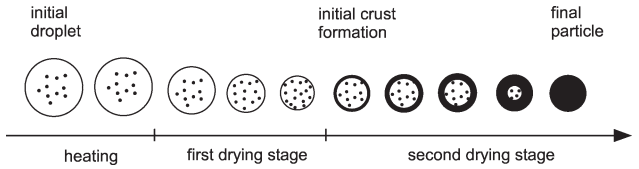

Figure 1. Drying stages of a droplet.

After an initial phase of heating, the first drying stage sets in where the liquid evaporates at a constant rate. Following the initial crust formation due to the suspended particles in the droplet the second drying stage starts with a thickness-dependent evaporation rate and leads to different final particle morphologies.

After a verification of the model results with data obtained from literature for special cases, we will investigate for example the influence of the aggregation kinetics (kernels) and the thermal conditions on the formed wet particle at the end of the first drying stage.

Mathematical Modeling

In the following, we consider a spherical droplet with radius R that is surrounded by a fluid phase, for example air (Figure 2). Inside this droplet solid nanoparticles are dispersed (spatially distributed). The interesting particle property will be their characteristic size ξ, for example, the diameter in case of spherical particles. The size and the spatial position $r \in [0, R]$ of the nanoparticles inside the droplet are of interest because many transport processes and process limitations depend on local spatial profiles. It is assumed that the droplet remains spherical (and symmetric with respect to the radial direction) and that no gradients in the angular direction exist. In this case one spatial coordinate (the radius) suffices to describe the spatial distribution of the nanoparticles in the interior of the droplet.

For the description of the solid phase processes the notion of a number density distribution $n\ (t,\ r,\ \xi)$, which describes the number of nanoparticles in the infinitesimal "volume" $[r,\ r + \Delta r] \times [\xi,\ \xi + \Delta\xi]$, is used.

The main focus of the following derivations lies on the temporal evolution of the number density distribution. It is affected by different processes – depicted in Figure 3: drying of the droplet, mass transfer of solid particles, and particle formation in the interior of the droplet. Whereas drying on its own leads to an increase in number density at the boundary of the droplet, diffusion induces a particle movement toward the center of the droplet that has an equalizing effect on the number density distribution. Particle formation also changes the number density distribution, for instance in aggregation the total number of particles decreases and larger particles are formed shifting the density distribution to higher particle sizes (and volumes).

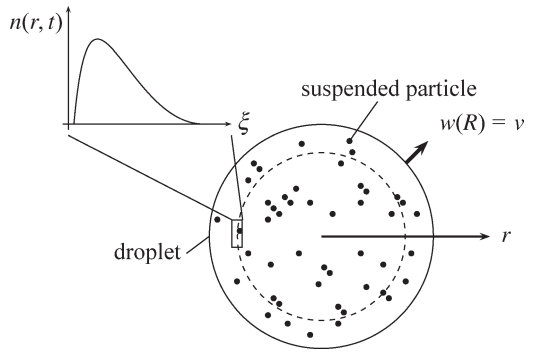

Figure 2. Set-up for the mathematical modeling of drying of a droplet.

Particles are dispersed in a droplet of (initial) radius R that is surrounded by a gas phase. Because of drying, the radius will shrink with a shrinking rate $w(R) = v$, that is, $R = R(t)$.

Using a standard population balance approach, compare, Ramkrishna,[5] the evolution can be described by

$$\frac{\partial n}{\partial t} = -\frac{1}{r^2}\frac{\partial}{\partial r}\left(r^2 j_r\right) - \frac{\partial j_\xi}{\partial \xi} + \sigma, \quad r \in (0,R],\ \xi \in [0,\infty), \quad (1)$$

where j_r denotes the flux of particles in direction of the radial coordinate, and j_ξ denotes the flux of the particles with respect to the property coordinate. The net rate of production σ accounts for all internal processes in the droplet that create new particles or consume particles, for example, aggregation and breakage. Note that in Eq. 1 the divergence operator with respect to r is written in spherical coordinates to account for the geometry of the droplet.

In the direction of the droplet radius r, we consider diffusion as the dominating transport phenomenon. The flux along this coordinate can therefore be written as

$$j_r = -D\,\frac{\partial n}{\partial r}, \quad (2)$$

where D is the diffusion coefficient of the solid in the liquid. For nanoparticles, it can be calculated by the Stokes–Einstein relation

$$D = \frac{k_B T_d}{6\pi\,\eta\,\xi}, \quad (3)$$

where k_B is the Boltzmann constant, T_d is the temperature of the droplet, and η denotes the dynamic viscosity of the liquid.

In terms of the particle size ξ we assume no change by fluxes, for example, growth, that is $j_\xi = 0$. However, we

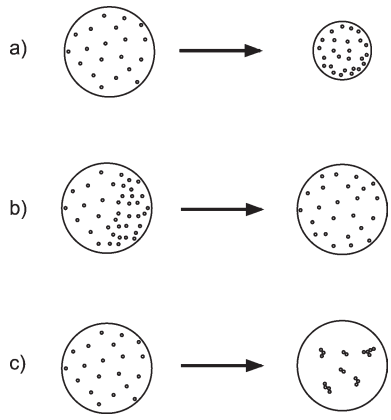

Figure 3. Main processes considered in this work affecting the dispersed nanoparticles in the droplet.

a) Drying of droplet leads to an increase in particle concentration at the boundary of the droplet; b) particle movement by diffusion equalizes the particle concentration over the droplet volume; c) particle formation due to aggregation (increase in particle volume and decrease in particle number).

consider the change of size by an internal process, that is, aggregation. The production term σ can then be expressed – under the assumption of spherical particles (using the particle volume $v \sim \xi^3$) – as

$$\sigma = \frac{1}{2}\int_0^v \beta^*(u, v-u)n(t,r,u)n(t,r,v-u)\,du - \int_0^\infty \beta^*(u,v)n(t,r,u)n(t,r,v)\,du. \quad (4)$$

In this formulation, β^* is the aggregation kernel for which various laws are available depending on the underlying process, for example, constant kernel, sum kernel, or shear kernel.

The population balance is then mathematically a 2-D partial-integro-differential equation, for which we pose the following boundary conditions

$$\lim_{r\to 0+} j_r(t,r,\xi) = 0, \quad (5)$$

$$j_r(t,R,\xi) = 0, \quad (6)$$

i.e., we assume no loss of solid particles in the droplet due to mass transport.

Assuming a uniform temperature θ_d an energy balance for the droplet yields[8]

$$\left(c_{p,wl}m_w + c_{p,s}m_s\right)\frac{d\theta_d}{dt} = h(\theta_g - \theta_d)4\pi R^2 - \dot{M}_{evap}\left(-c_{p,wl}\theta_d + \Delta h_{evap} + c_{p,wg}\theta_g\right). \quad (7)$$

Here, θ_g denotes the temperature of the surrounding gas phase, Δh_{evap} is the specific evaporation enthalpy, and m_w and m_s are the masses of water and solid in the droplet, respectively. In the calculation of the evaporation, the liquid in the droplet is first cooled down to $\theta_{evap} = 0°C$ ($-c_{p,wl}\theta_d$), then it is evaporated at this temperature (Δh_{evap}) and then the vapor is heated up to the gas temperature ($c_{p,wg}\theta_g$). The benefit is that only one constant specific heat of evaporation (which is available from tables) is required for the calculation.

The heat transfer coefficient h is given by Renksizbulut and Yuen[14]

$$h = \frac{\mathrm{Nu}\,k_g}{2R}, \mathrm{Nu} = (2 + 0.6\,\mathrm{Re}^{1/2}\mathrm{Pr}^{1/3})(1+\mathrm{B})^{-0.7}. \quad (8)$$

In this equation, $\mathrm{B} = c_{p,wg}(T_g - T_d)/\Delta h_{evap}$ denotes the so called Spalding number which accounts for the influence of the Stefan flow in the boundary layer around the droplet.

As the droplet is drying its radius will shrink with a certain rate v, that is, the radius of the droplet is a function of time: $R = R(t)$. Considering the first drying period only, that is, no crust formation by solid particles, and assuming a uniform shrinkage, that is, the droplet remains spherical, a mass balance for the liquid in the droplet yields

$$\frac{dR}{dt} = v = -\frac{\varrho_g}{\varrho_l}\beta_{lg}(R)(Y_{sat} - Y_g), \quad R(t_0) = R_0, \quad (9)$$

where R_0 is the radius of the droplet just before the drying starts, and β_{lg} is the mass transfer coefficient from the liquid to the gas phase. It can be calculated by

$$\beta_{lg} = \frac{\mathrm{Sh}\,\delta_g}{2R}, \quad (10)$$

with Sh the dimensionless Sherwood number, given by Renksizbulut and Yuen[14]

$$\mathrm{Sh} = \left(2 + 0.6\,\mathrm{Re}^{1/2}\mathrm{Sc}^{1/3}\right)(1+\mathrm{B})^{-0.7}, \quad (11)$$

and δ_g the diffusion coefficient of water vapour in the gas. It can be calculated from a relation given by Grigoriev and Zorin[15]

$$\delta_g = 3.546 \times 10^{-10}\frac{\mathrm{m}^2}{\mathrm{K}^{1.75}\,\mathrm{s}} \times \left(T_d + T_g\right)^{1.75}, \quad (12)$$

with $[T_g] = [T_d] = \mathrm{K}$ and $[\delta_g] = \mathrm{m^2 s^{-1}}$.

The driving force for the mass transfer is given by the difference in moisture contents of the surrounding gas phase ($Y_{sat} - Y_g$), which is a measure for the capability of the gas to further absorb liquid. The saturation moisture content Y_{sat} is the maximum amount of liquid that can be absorbed per kilogram of gas. This value depends on the temperature of the gas θ_g and has to be calculated from

$$Y_{sat} = 0.622\frac{p_{sat}}{p - p_{sat}}, \quad p_{sat} = \exp\left(A^* - \frac{B^*}{C^* + \theta_g}\right), \quad (13)$$

with $[p_{sat}] = \mathrm{Pa}$, $[\theta_g] = °\mathrm{C}$ and the empirical Antoine constants $A^* = 23.4588$, $B^* = 3977.3782°\mathrm{C}^{-1}$, and $C^* = 233.3172°\mathrm{C}$.

This modeling approach, however, is only valid for arbitrary but constant balance volumes, that is, the influence of the drying droplet – the shrinkage in (balance) volume – on the number density distribution is not yet accounted for.

There are several ways to account for the changes in the number density distribution induced by the drying. Handscomb et al.[11] (amongst others) modeled the influence by an artificial boundary source term at $r = R(t)$. Although this yields a consistent formulation of the problem in the cases they considered (diffusion along the radial axis of the droplet), it complicates the handling of processes where no transport by diffusion is involved, for instance drying and aggregation of particles only. In Handscomb et al.,[11] the natural boundary condition at $r = R(t)$, as posed by the diffusion, is not present in the formulation of the process and has to be included manually.

The present work starts with the integral formulation of the PBE for a time-varying balance volume. An application of Leibniz' rule yields an additional term that accounts for the local change in number density due to a local change of the balance volume. The corrected PBE then reads

$$\frac{\partial n}{\partial t} + \frac{1}{r^2}\frac{\partial}{\partial r}(r^2 nw) = -\frac{1}{r^2}\frac{\partial}{\partial r}\left(r^2 j_r\right) + \sigma, \quad r \in (0, R(t)],\ \xi \in [0,\infty) \quad (14)$$

Here, $w = w(r)$ is the local shrinkage rate of the balance volume in radial direction. It has only a non-zero value at the current boundary $r = R(t)$, that is, $w(R) = v$, as only here the shrinkage occurs. To guarantee mass conservation of solid particles, the boundary conditions have to be formulated as follows

$$\lim_{r\to 0+} j_r(t,r,\xi) = 0, \quad (15)$$

$$\left(-D\,\frac{\partial n}{\partial r}\right)\Big|_{r=R(t)} = 0. \tag{16}$$

The new term in the PBE can be interpreted as a convective flux of solid particles along the radial direction caused by the shrinking droplet volume. Note, that this formulation is independent of the presence of a diffusive process – the new boundary term stems from the newly introduced convection. The formulation also paves the way for the consideration of nonuniform shrinkage by allowing for a local shrinkage rate, but this is out of the scope of the current investigation.

The equations presented constitute a complete model to simulate the temporal evolution of the number density distribution. The present "moving boundary"[16] or "receding interface" problem[11] is computationally difficult due to the different time scales of the subprocesses drying, diffusion, and aggregation and the presence of two distributed coordinates (particle size and position).

In the following section, we present simulation results for the temporal evolution of the number density distribution for several important cases. After a validation of the mass and energy balance part of the model by comparison with experimental data, we examine how the number density profiles are affected by the various subprocesses, starting with the limiting case of pure drying. Afterward, we briefly consider the combined subprocesses drying and diffusion, before focussing on the case of drying, diffusion, and aggregation. Here, the influence of the aggregation kinetics on the profiles, the locking point, and the resulting droplet porosity at the end of the first drying stage is investigated in detail.

Simulation Results

To simulate the model equations numerically the PBE is discretized with respect to the external and internal coordinates. Here, N_r nodes in radial direction of the droplet, and N_ξ nodes in direction of the property coordinate are used. The discretization interval of the property coordinate ξ and the number of nodes is chosen such that the total volume of particles in the droplet is predicted consistently, that is, no loss of total volume due to creation of particles outside the discretized interval occurs. For the discretization of the convection and the diffusion term, a finite volume method is used. The integral term used to describe the aggregation process is discretized by an application of the Cell Average method.[17]

To avoid numerical difficulties due to the different orders of magnitude in the discretized property distribution and the droplet radius, we introduce the following scalings

$$r = R(t)\,\gamma, \quad \gamma \in [0,1], \tag{17}$$

$$n = N(t)\,\chi, \quad \chi \in [0,1], \tag{18}$$

with R the droplet radius, and $N = 3\mu_{00}(t)/(4\pi R^3)$ the total number concentration of particles. Note that by introducing these scalings the new quantities γ and χ are dimensionless.

The resulting set of ordinary differential equations for the discretized number density distribution and the droplet radius can then be cast into the form

$$\dot{x} = f(x,p), \quad x(t_0) = x_0, \tag{19}$$

where $x \in \mathbb{R}^{N_r N_\xi + 1} = [\chi_{1,1}, \ldots, \chi_{N_r,N_\xi}, \gamma]^{\mathrm{T}}$, and p is the vector of process parameters.

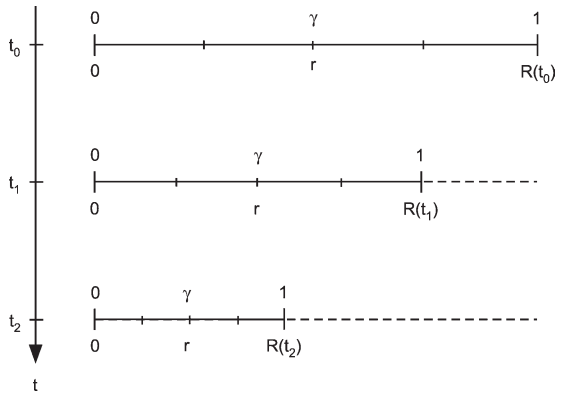

Figure 4. Illustration of the general idea of the moving grid implementation.

In each time step of the simulation the remaining droplet radius is discretized equally into N_r control volumes. The velocity of the grid is equal to the drying velocity of the droplet.

To discuss the results qualitatively we introduce the notion of a moment of a multivariate distribution

$$\mu_{i,j}(t) = \int_0^{R(t)} \int_0^{\infty} r^i\,\xi^j n(t,r,\xi)\,\mathrm{d}\xi\,\mathrm{d}r. \tag{20}$$

Of particular interest are the moments $\mu_{2,0}$, $\mu_{2,1}$, $\mu_{2,2}$, and $\mu_{2,3}$ as they directly relate to the total number, total length, total surface area, and total volume (mass) of the particles inside the droplet. Note, that the index i is equal to 2 to account for the spatial geometry of the droplet.

The differential equations are implemented (in radial direction) on a moving grid. The general idea is depicted in Figure 4 and allows for a good representation of the movement of particles in the interior of the droplet with just a few control volumes. The equations are integrated by MATLAB's ode15s solver that uses a variable-order numerical differentiation scheme.[18]

Contrary to other models (e.g., Mezhericher et al.[10]) all phenomena included in the model (drying, diffusion, and aggregation, see Eq. 14) can be switched on or off. Thus, it is possible to investigate for example only drying or drying plus aggregation without diffusion with one and the same model.

Model validation by selected experimental data

Before investigating the influence of different parameters on the drying process and concentration profiles within the droplet, the overall heat and mass balances are validated. Therefore, the model is compared with experimental data from literature (Nešić and Vodnik[8]). In the experiments of Nešić and Vodnik, a droplet ($R_{\mathrm{d},0} = 1$ mm) containing nanoscaled silica particles of 16 nm in diameter was dried in a controlled air stream with a temperature of 178°C and a gas velocity of 1.4m s^{-1}. The density of solid ϱ_{s} was calculated using the corresponding initial experimental conditions

$$\varrho_{\mathrm{s}} = \frac{m_{\mathrm{s},0}}{V_{\mathrm{s},0}}, \tag{21}$$

where $m_{\mathrm{s},0}$ is the initial mass of solid and $V_{\mathrm{s},0}$ the initial solid volume. The initial solid mass can be calculated from the initial solid mass fraction $\omega_{\mathrm{s},0}$ and initial droplet mass $m_{\mathrm{d},0}$

Table 1. Experimental Data from Nešić and Vodnik[8]

Initial droplet radius (mm)	$R_{d,0}$	1
Size of primary particles SiO_2 (spherical; nm)	ξ_{PP}	16
Density of solid (kg m^{-3})	ϱ_s	939
Initial solid mass content ($kg_s\ kg_d^{-1}$)	$\omega_{s,0}$	0.3
Initial droplet mass (g)	$m_{d,0}$	4.3×10^{-3}
Gas temperature (°C)	θ_g	178
Gas velocity (m s^{-1})	u_g	1.4
Initial droplet temperature (°C)	$\theta_{d,0}$	19
Relative humidity of gas bulk	ϕ	0.004
Density of liquid (kg m^{-3})	ϱ_l	1000
Density of gas (kg m^{-3})	ϱ_g	1

$$m_{s,0} = \omega_{s,0} m_{d,0}. \tag{22}$$

The initial solid volume is computed from the initial droplet volume $V_{d,0}$ and the initial liquid volume $V_{l,0}$ inside the droplet using the following equation

$$V_{s,0} = V_{d,0} - V_{l,0},\ V_{d,0} = \frac{4}{3}\pi R_{d,0}^3, \tag{23}$$

$$V_{l,0} = m_{l,0}/\varrho_l = (1 - \omega_{s,0})\, m_{d,0}/\varrho_l. \tag{24}$$

Here, $R_{d,0}$ is the initial droplet radius and ϱ_l the density of water. Applying these equations to the experimental data of Nešić and Vodnik yields a solid density of $\varrho_s = 939$ kg m^{-3}. This is an untypical value for the density of silica, but is used nevertheless in the following calculations for best comparison of overall mass and temperature history with the experimental data. The data used for the simulation and comparison is summarized in Table 1.

According to Nešić and Vodnik the following diffusion coefficient was used:

$$D = \begin{cases} 10^{-7}\,\mathrm{m^2\,s^{-1}}, & \omega_l > 0.6, \\ 1\,\mathrm{m^2\,s^{-1}} \times \exp\left(-\frac{28.1+282\omega_l}{1+15.47\omega_l}\right), & \omega_l \le 0.6 \end{cases}. \tag{25}$$

Here, ω_l is the mass fraction of liquid inside the droplet. In this correlation, a value for the diffusion coefficient equal to 10^{-7} $m^2 s^{-1}$ was assumed to model a vigorous internal circulation within the droplet caused by air drag force before the gel structure is formed, as it was experimentally observed by Nešić and Vodnik. Note, that for validation, aggregation is not considered and the diffusion coefficient is not particle size dependent.

The moment when the local porosity $\varepsilon_{sh} = 1 - V_{agg}/V_{sh}$ in the outer shell (Figure 5), where V_{agg} is the total volume of the aggregates and V_{sh} is the total volume of the shell, decreases to a value of $\varepsilon_{sh} \le 0.4$ local crust formation is initiated. This moment is the so called locking point. Then, the droplet no longer dries with the first drying period rate but with the second drying period rate, which is limited by the characteristics of the formed layer.

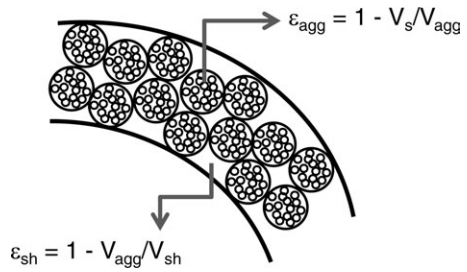

Figure 5. Schematic of shell porosity.

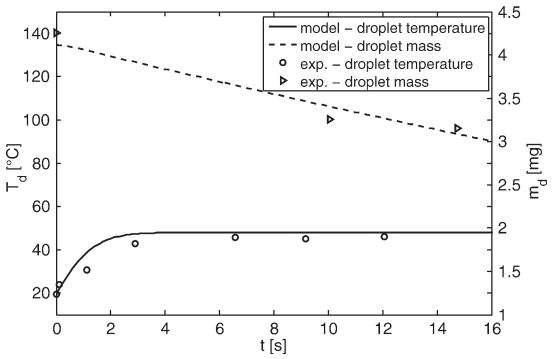

Figure 6. Temporal evolution of droplet mass (right-hand axis) and droplet temperature (left-hand axis) in the first drying stage and comparison with experimental data from Nešić and Vodnik.[8] $\theta_g = 178°C, u_g = 1.4\ m\ s^{-1}, R_{d,0} = 1$ mm.

In Figure 6, the predicted evolution of silica droplet mass and temperature and the corresponding experimental values of Nešić and Vodnik in the first drying stage are shown. As one can see, there is a good agreement between the simulated curves and experimental points for both droplet temperature and droplet mass.

After validation of the overall heat and mass balance, we can consider how the concentration profiles inside the droplet may look like (Figure 7): At the beginning there is a uniform concentration profile inside the droplet. With increasing time the radius of the droplet decreases due to drying, leading to an increase of the total number concentration in the outer volume. Because of the resulting concentration gradient, the particles are transported by diffusion in direction of the radial coordinate from the droplet boundary to the droplet center leading to an increase in total number concentration in the inner volumes. After gel formation, the diffusion coefficient decreases (Eq. 25), that is, the particles do have a lower mobility, leading to a higher increase of the concentration profile at the droplet boundary due to drying.

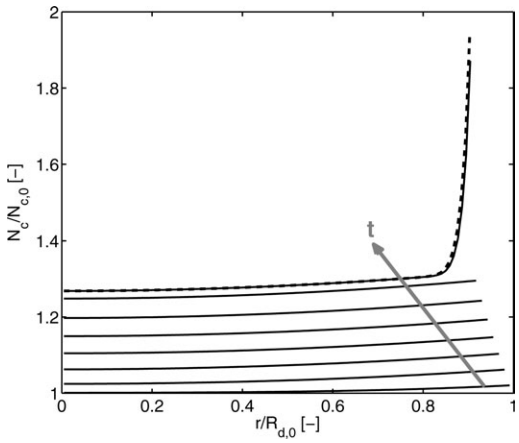

Figure 7. Normalized number concentration profiles inside silica droplet.

Curves are plotted every 2 s. The dashed line determines the concentration profile at the locking point ($t_{lock} = 16.2$ s).

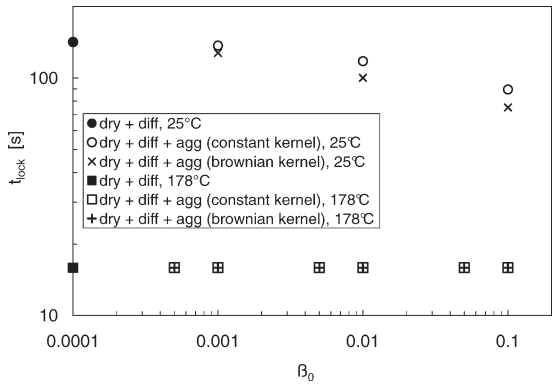

Figure 8. Influence of aggregation kernel and gas temperature (θ_g = 178°C and θ_g = 25°C) on the locking point.

For diffusion the Stokes–Einstein equation is used. If the drying is very fast, aggregation has no significant influence on the locking point.

Influence of aggregation on the drying process

The graphs in Figure 7 give a first idea how the concentration profile in a suspension droplet drying under certain conditions may look like. Different particle phenomena can have an influence on the drying process and the resulting concentration profiles within the droplet. Our special interest concerns the influence of aggregation on the drying process as this has not yet been studied.

To investigate the influence of aggregation on the drying process, the Stokes–Einstein equation is used to calculate the diffusion coefficient (Eq. 3). In Figure 8, computational results for the locking point, meaning the time when the solid volume fraction at droplet surface reaches a value of 0.6 or $\varepsilon_{sh} = 0.4$, for two different gas temperatures and different aggregation kernels are shown: first, we consider a constant aggregation kernel $\beta^*(u, v) = \beta_0$ due to its simplicity. However, as this kernel does not necessarily reflect the true aggregation behavior of nanoparticles, we also consider the Brownian kernel $\beta^*(u, v) = \beta_{0,B}(2 + u/v + v/u)$. This has been used in various publications, for instance Gharagozloo and Goodson[13] and Tourbin and Frances.[19]

Using an approximation of the continuum Brownian kernel for the collision of equal-sized particles, the aggregation efficiency $\beta_{0,B}$ can be related directly to the temperature of the particle and the dynamic viscosity of liquid in the droplet via Boltzmann's constant k_B

$$\beta_{0,B} = \frac{8k_B}{3\eta}(\theta_d + 273.15). \tag{26}$$

In comparision to the constant kernel, it can be said that for values $\beta_0 < \beta_{0,B}$ the collisions are inhibited for instance by long-range repulsive forces or are not totally efficient due to the contact dynamics. For values $\beta_0 > \beta_{0,B}$ the long-range forces are attractive, assisting the formation of aggregates.

In the following, we assume values for the aggregation kernels that allow for a sufficiently fast aggregation of particles in comparison to the drying of the droplet. If aggregation is very slow compared to drying then the process is dominated by drying and the results will be similar to the case of drying only.

Using the same value for the aggregation efficiency in both kernels ($\beta_0 = \beta_{0,B}$), which for the Brownian kernel is several orders of magnitude larger then the threshold value calculated by Eq. 26 signaling a highly unstable nanosuspension, one obtains the results shown in Figure 8. For both kernels an influence of the aggregation efficiency on the locking points can be observed, that is, they follow the same trend. However, quantitatively the results cannot be compared directly in this graph. Here the contribution of the size-dependent part of the kernel has to be included, to find the corresponding aggregation efficiencies

$$\beta_0 = \beta_{0,B}(2 + u/v + v/u). \tag{27}$$

Here, one sees that for instance for particles with $u \approx v$: $\beta_0 = 4\beta_{0,B}$, that is, for a quantitative comparison of the results the curve for the constant kernel has to be shifted to the left to be comparable with the Brownian kernel. If one performs this operation (not depicted), one observes that both graphs almost coincide, that is, the contribution of the size-dependent term is almost negligible. For that reason, we restrict ourselves in the following discussion to the constant aggregation kernel. This simplification yields a correct representation of the trend for the Brownian kernel, however, for a quantitative comparison the information has to be scaled by the size-dependent part.

There is a significant influence of the drying rate, represented by the different gas temperatures, on the time of crust formation. Higher drying rates lead to a faster contraction of the droplet and a faster increase of solid concentration at the droplet surface so that the maximum value of solid volume fraction of 0.6 is achieved faster.

For fast drying, there is no significant influence of aggregation on the locking point. This can be explained as follows: the faster the drying the earlier the locking point is achieved, that is, the faster the immobile crust is formed. Thus, for fast drying, the particles have hardly time to diffuse from the droplet surface to the droplet center. Consequently, the size of the diffusion coefficient has hardly an influence on the time of crust formation, and thus, there is no influence by the change in diffusion coefficient due to the particle growth caused by aggregation.

Contrary to that, in the case of slow drying, particles have more time to diffuse from the droplet surface to the droplet center whereby smaller particles are transported faster than bigger ones (Eq. 3). Thus, a higher aggregation kernel and the resulting bigger aggregates are leading to slower diffusion of the particles and therefore to a decrease in locking point as the maximum value of solid volume fraction of 0.6 is achieved faster.

As shown in Figure 8, the influence of aggregation on the time of crust formation can be very interesting. We will now consider, step by step, how the concentration profiles change under the influence of diffusion and aggregation. We start with drying only, then diffusion is considered additionally. The final case will be the combined process of drying, diffusion, and aggregation. In all cases, the process parameters listed in Table 2 are used.

Case 1: Drying of Droplet. As already mentioned, with the present formulation of the model (Eq. 14), it is possible to determine the influence of the single effects of drying, diffusion, and aggregation individually with one and the same model by just activating the subprocesses. Thus, it is possible to consider the case of pure drying. In previous works (e.g., Refs. 9–11), the problem of the moving boundary (i.e.

Table 2. Simulation Parameters

Initial droplet radius (mm)	$R_{d,0}$	1
Size of primary particles SiO_2 (spherical; nm)	ξ_{PP}	1
Density of solid (kg m^{-3})	ϱ_s	939
Initial solid mass content ($kg_s\ kg_d^{-1}$)	$\omega_{s,0}$	0.1
Gas temperature (°C)	θ_g	25
Gas velocity (m s^{-1})	u_g	1.4
Initial droplet temperature (°C)	$\theta_{d,0}$	19
Relative humidity of gas bulk	ϕ	0.004
Density of liquid (kg m^{-3})	ϱ_l	1000
Density of gas (kg m^{-3})	ϱ_g	1
Number of discrete radial volume elements	N_r	100
Number of discrete size classes	N_ξ	14

the drying) is solved by modifying the boundary condition for the diffusion term. But in those formulations, without diffusion ($D = 0$), there is no boundary condition and therefore, it is a problem to handle the case of pure drying.

In the case of pure drying, the particles are moved just by contraction of the droplet, there are no other transport processes (e.g., diffusion). At each time step the remaining droplet volume is rediscretized into N_r control volumes. The size of each of these control volumes is decreased by this action as the radius of the droplet is shrinking. The volume of solid in each of these volume elements is also changed by the rediscretization. A certain fraction is now accounted to the neighboring volume due to the "shifting" of the coordinate system. In total, the number of particles in each inner volume decreases so that the number concentration in each of these volume elements remains at its initial value. The "shifted" particles end up in the (moving) outer shell where they accumulate due to the boundary conditions stated, leading to an increase of number concentration in the outer shell.

In Figure 9, the temporal evolution of the concentration profiles inside the droplet is shown. At the beginning of the process there is a uniform concentration profile inside the droplet. Then, the number concentration in the outer shell increases due to drying and the corresponding decrease in volume. The curves are getting shorter due to the shrinkage of the droplet. The number concentration in the inner volume elements remains constant.

An inspection of the numerical results for the size distribution shows that the first four total moments [μ_{2i}, (i = 0,…,3)] of the distribution are constant: as there is no transport of solid particles out of the droplet, that is, the total mass of solid inside the droplet is conserved, the third moment remains at its initial value. The total moment μ_{20}, representing the total number of particles, remains constant as well as there is no particle formation process (no aggregation). Similarly, the first and the second moment, which correspond to the total length and total surface area of the particles, are constant.

Case 2: Drying and Diffusion. Similar to Case 1, there are no particle formation processes, only the diffusive transport of particles in direction of the radial coordinate. As this transport effect does not have any influence on the total moments they are conserved during the process.

Because of the concentration gradient, caused by the increase of number concentration in the outer shell due to shrinkage of the droplet (Case 1), the particles are transported by diffusion from the droplet boundary to the droplet center. The diffusion process leads to an equalization of the particle number concentration along the radial coordinate, and thus, the time of the locking point increases because it takes longer to build up the critical solid content in the outer shell.

Two limiting cases can be acquired: first, if the diffusion process is very slow compared to the drying, the particles do not have enough time to equalize the concentration gradient caused by drying. In this case, one would obtain concentration profiles similar to those of Case 1 (pure drying). Conversely, if the diffusion process is very fast compared to the drying, this leads to a complete equalization of the number concentration along the radial coordinate. In this case, one would obtain horizontal concentration profiles and a further increase in the locking point.

The temporal evolution of the concentration profile for a case in between these two limits, where the diffusive transport is slow compared to drying, is shown in Figure 10. Here, one observes an equalizing effect of the diffusion on the profile (Figure 9), but the diffusion is not fast enough to counteract the increase caused by the shrinkage of the

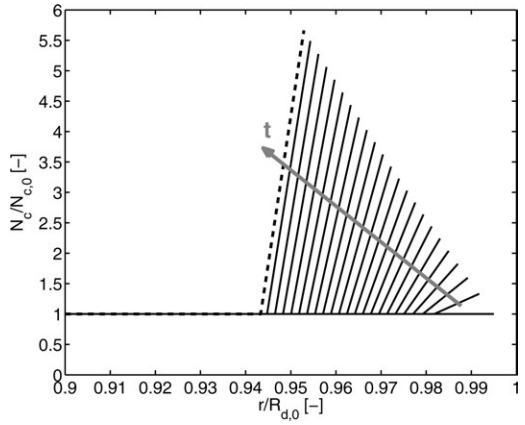

Figure 9. Evolution of concentration profiles for the case of pure drying.

Curves are plotted every 2 s. The dashed line determines the concentration profile at the locking point (t_{lock} = 43.6 s). Particles move just by contraction of the droplet, particle number concentration in (moving) outer shell increases.

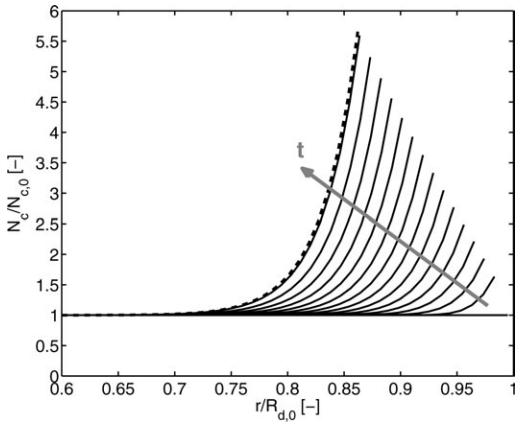

Figure 10. Evolution of concentration profiles for the case of drying and slow diffusion (see text).

Curves are plotted every 10 s. The dashed line determines the concentration profile at the locking point (t_{lock} = 141.7 s). Diffusion leads to an equalization of concentration along the radial coordinate.

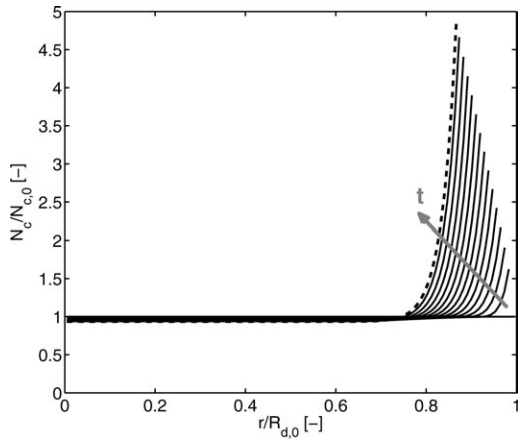

Figure 11. Evolution of concentration profiles for the case of drying, diffusion, and aggregation with constant aggregation kernel, $\beta_0 = 0.001$.

Curves are plotted every 10 s. The dashed line determines the concentration profile at the locking point ($t_{lock} = 136.9$ s).

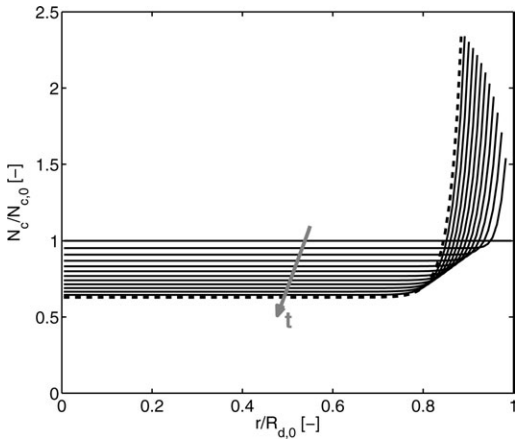

Figure 12. Evolution of concentration profiles for the case of drying, diffusion, and aggregation with constant aggregation kernel, $\beta_0 = 0.01$.

Curves are plotted every 10 s. The dashed line determines the concentration profile at the locking point ($t_{lock} = 117.8$ s). A higher aggregation kernel leads to a decrease of number concentration in the inner volume elements (cf., Fig. 11).

droplet. In comparison with the case of drying only, an increase in the locking time t_{lock} can be observed.

Case 3: Drying, Diffusion, and Aggregation. In this case, larger particles are formed from smaller ones by aggregation leading to a decrease in total particle number and particle number concentration, respectively. The aggregates are transported by diffusion due to the concentration gradient caused by the drying of the droplet (Case 2). As the mobility of the nanoparticles depends on their size (Eq. 3) aggregation and diffusion are linked, that is, smaller aggregates are transported faster than bigger ones. For the simulations, a constant aggregation kernel is used, that is, $\beta^* = \beta_0$. Simulations done with other aggregation kernels (e.g., brownian) show similar results.

The simulation results for three different aggregation kernel values are shown in Figures 11–13: the temporal evolution of the concentration profile for $\beta^* = \beta_0 = 0.001$ is depicted in Figure 11. Despite aggregation, the particle number concentration in the outer volume elements is increasing with increasing time, leading to the result that, for this aggregation kernel, drying is the dominating process, that is, the aggregation is slow compared to the drying. If the aggregation kernel is increased ($\beta^* = \beta_0 = 0.01$) the number concentration in the inner volumes decreases with increasing time (as shown in Figure 12) and, as can be observed in Figure 13, for $\beta^* = \beta_0 = 0.1$, the particle number concentration decreases even at the boundary of the droplet, even though drying promotes an increase of particle number concentration in the outer shell, that is, the aggregation is fast compared to drying and diffusion.

As the mobility of the particles depends on their size, for example, smaller particles are transported faster than bigger ones, the locking point decreases with increasing aggregation kernel (see also Table 3) due to the limited mobility of the particles.

As mentioned earlier, the aggregation process leads to a decrease of total particle number, represented by the zeroth moment μ_{20}. Accordingly, the total length (proportional to μ_{21}), and total surface area (proportional to μ_{22}) are also decreasing. As the total mass of particles inside the droplet is conserved, that is, no particles leave the droplet, the total third order moment μ_{23} of the distribution remains constant.

In Figure 14, the temporal evolution of the total zeroth moment until the locking point for the three constant aggregation kernels is shown. As one can see, higher aggregation rates are leading to a faster decrease in total particle number. In Figure 15, the radial distribution of the mean diameter inside the droplet at the time of the locking point is shown. Here, one can see that higher aggregation kernels are leading to bigger aggregates. In the outer volume elements, the size of the aggregates is increasing. This is due to the increase of particle number concentration in the outer volume elements caused by drying.

Finally, in Figure 16, the porosity profiles at the time of the locking point are shown. The porosity in the outer

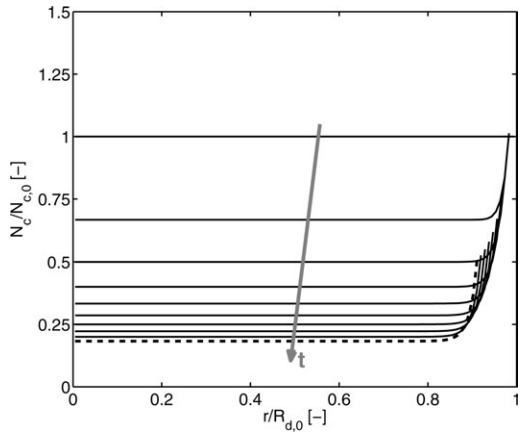

Figure 13. Evolution of concentration profiles for the case of drying, diffusion, and aggregation with constant aggregation kernel, $\beta_0 = 0.1$.

Curves are plotted every 10 s. The dashed line determines the concentration profile at the locking point ($t_{lock} = 89.5$ s). Decrease of number concentration even in the outer shell.

Table 3. Influence of the Different Subprocesses on the Locking Point

Case	Locking Point (s)
Drying only	43.6
Drying and diffusion	141.7
Drying, diffusion, and aggregation ($\beta_0 = 0.001$)	136.9
Drying, diffusion, and aggregation ($\beta_0 = 0.01$)	117.8
Drying, diffusion, and aggregation ($\beta_0 = 0.1$)	89.5

volume elements decreases due to the increase of particle number concentration caused by drying. The decrease of porosity in the outer volume elements gets steeper with increasing aggregation kernel. As bigger particles are transported slower than smaller ones, there is a minor compensation of particle concentration and thus in porosity, too.

In Figure 8 it was shown, that aggregation can have an influence on the drying process. The numerical results for the locking point, for the three case studies are summarized in Table 3.

For pure drying, the locking point is the lowest as there is no equalization of concentration by diffusion. Thus, the solid volume fraction at droplet surface reaches a value of 0.6 very fast. The diffusion process in the case of drying and diffusion leads to an equalization of number concentration along the radial coordinate and thus, to a decrease of particle concentration in the outer volume. Consequently, it lasts longer to reach a solid volume fraction of 0.6 at the droplet surface, and thus, one gets a higher locking point.

If aggregation is considered additionally, the locking point decreases again. Because of particle growth by aggregation and the resulting decrease in the diffusion coefficient (Eq. 3), the mobility of the particles is decreased. The higher the aggregation rates the faster the particles are growing and consequently the more the mobility of particles is decreased leading to faster achievement of the locking point.

There are two limiting cases: if the aggregation process is very slow, the mobility of particles is hardly restricted. For this case, the time of the locking point is similar to the one of drying and diffusion. If the aggregation is very fast, the mobility of particles is intensively restricted. Then, the time of the locking point converges to the one of pure drying.

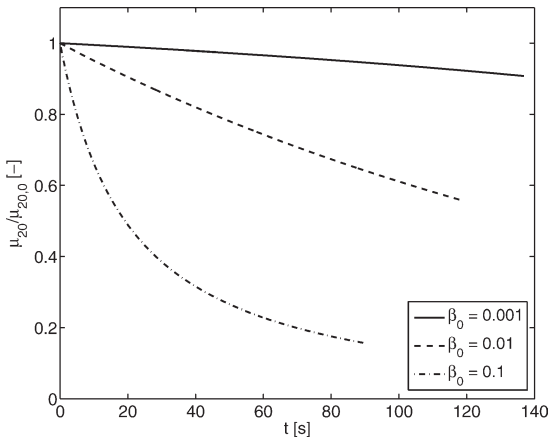

Figure 14. Evolution of the total moment μ_{20} for the case of drying, diffusion, and aggregation.

A constant aggregation kernel is used. Curves end up at the locking point. Higher aggregation kernels are leading to a decrease of the locking point and to a faster decrease in particle number.

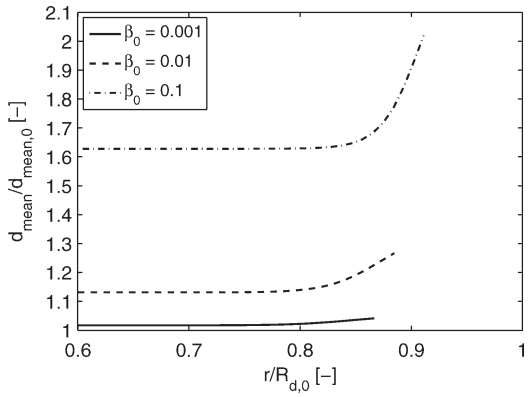

Figure 15. Profile of the mean diameter of the particles inside the droplet at the time of crust formation for the case of drying, diffusion, and aggregation.

A constant aggregation kernel is used. The size of the aggregates is increasing mainly near the outer shell.

Conclusions and Outlook

In this work, we presented a mathematical model to describe the simultaneous processes of drying, diffusion, and aggregation of nanoparticles suspended in liquid droplets. The considered properties of the particles are the current position inside the droplet and their characteristic size. As the radius of the droplet shrinks with the drying, the time evolution of the particle size distribution is stated as a moving boundary problem. In contrast to previous contributions, for example Handscomb et al.,[11] the effect of shrinking on the PBE was not modeled as an artificial boundary source but as a flux term in the PBE which is more suitable for important limiting cases, for example, pure drying of the droplet.

The model was validated for the case of drying and diffusion using experimental data from Nešić and Vodnik.[8] The

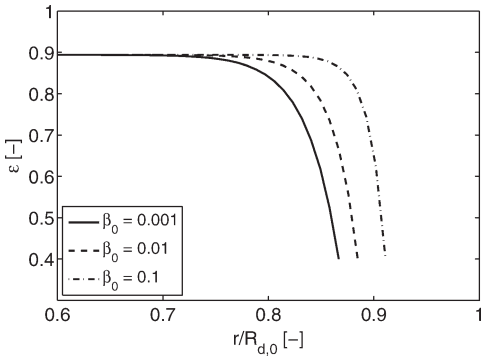

Figure 16. Porosity profiles at the time of crust formation for the case of drying, diffusion, and aggregation.

A constant aggregation kernel is used. Higher aggregation kernels are leading to a steeper decrease of porosity toward the outer shell.

results show a good agreement between the experimental and simulated data.

Additionally, simulations were conducted for certain limiting cases: drying only, and drying and diffusion. The conservation of the zeroth and third total moment of the size distribution serve as a verification of the model.

In the final case the processes drying, diffusion, and aggregation are combined. For this case the evolution of characteristic values, for example, the total moments of the distribution or the particle number concentration, was shown. The combined case was simulated for different aggregation kernels to illustrate the influence of aggregation on the drying process and the locking point. The faster the aggregation is compared to drying and diffusion, the earlier the locking point is achieved. It was also shown that the resulting droplet porosity is influenced by the speed of aggregation.

Up until now, all results are limited to the first drying stage, meaning the time before an immobile crust at the droplet surface is formed. Next will be the extension of the model to the second drying stage and considering the processes after crust formation. Also, drying experiments by means of ultrasonic levitation will be realized.

Acknowledgments

The authors gratefully acknowledge the funding of this work by the German Federal Ministry of Science and Education (BMBF) as part of the InnoProfile project NaWiTec and of the German Israeli Foundation for Scientific Research and Development (GIF). They also gratefully acknowledge the comments of an anonymous reviewer that helped to improve the interpretation of the aggregation kinectics.

Notation

Symbols

A^* = Antoine constant
B^* = Antoine constant ($^\circ C^{-1}$)
C^* = Antoine constant ($^\circ C$)
c_p = specific heat capacity (J kg^{-1}K^{-1})
Δh_{evap} = specific evaporation enthalpy (J kg^{-1})
d = diameter (m)
D = diffusion coefficient of particles in liquid (m^2 s^{-1})
h = heat transfer coefficient (W m^{-2} K^{-1})
j_r, j_ξ = flux density (m^{-3} s^{-1})
k_B = boltzmann constant (J K^{-1})
k = heat conductivity (W m^{-1} K^{-1})
m = mass (kg)
n = number distribution density (m^{-3} m^{-1})
N_c = number concentration in radial volume (m^{-3})
p = pressure (N m^{-2})
r = external coordinate (radius) (m)
R = droplet radius (m)
t = time (s)
T = temperature (K)
u = velocity (m s^{-1})
u,v = volume of particles (m^3)
V = volume (m^3)
w = local shrinkage rate (m s^{-1})
Y = moisture content (kg$_w$ kg$_g^{-1}$)

Dimensionless Numbers

B = Spalding number
Nu = Nusselt number
Pr = Prandl number
Re = Reynolds number
Sh = Sherwood number

Greek letters

β = mass transfer coefficient (m s^{-1})
β_0 = aggregation efficiency (s^{-1})
β^* = aggregation kernel (Various)
γ = dimensionless radius
δ_g = diffusion coefficient of water vapour in gas (m^2 s^{-1})
ε = porosity
η = dynamic viscosity of droplet (kg m^{-1} s^{-1})
θ = temperature ($^\circ C$)
μ_{2j} = j-th total moment (j = 0,1,2,3) (m^j)
ξ = internal coordinate (m)
ϱ = mass density (kg m^{-3})
σ = net rate of production (m^{-2} s^{-1})
ϕ = relative humidity
χ = dimensionless number density
ω = mass fraction (kg kg$_d^{-1}$)

Subscripts

0 = initial value (t = 0)
agg = agglomerate
B = brownian
d = droplet
evap = evaporation
i,j = order of moments
g = gas
l = liquid
lg = from liquid to gas phase
lock = locking point
mean = mean value
n = normalized
PP = primary particle
s = solid
sh = shell
sat = saturation
w = water
wg = gaseous water
wl = liquid water

Literature Cited

1. Chaubal M, Popescu C. Conversion of nanosuspensions into dry powders by spray drying: a case study. *Pharm Res*. 2008;25:2302–2308.
2. Ranz WE, Marshall WR Jr. Evaporation from drops. *Chem Eng Prog*. 1952;48:141–180.
3. Walton DE. The evaporation of water droplets: a single droplet drying experiment. *Drying Technol*. 2004;22:431–456.
4. Hulburt HM, Katz S. Some problems in particle technology: a statistical mechanical formulation. *Chem Eng Sci*. 1964;19:555–574.
5. Ramkrishna D. *Population Balances: Theory and Application to Particulate Systems in Engineering*. New York: Academic Press, 2000.
6. Charlesworth D, Marshall W Jr. Evaporation from drops containing dissolved solids. *AIChE J*. 1960;6:9–23.
7. Sano Y, Keey R. The drying of a spherical particle containing colloidal material into a hollow sphere. *Chem Eng Sci*. 1982;37:881–889.
8. Nešić S, Vodnik J. Kinetics of droplet evaporation. *Chem Eng Sci*. 1991;46:527–537.
9. Seydel P, Blömer J, Bertling J. Modeling particle formation at spray drying using population balances. *Drying Technol*. 2006;24:137–146.
10. Mezhericher M, Levy A, Borde I. Heat and mass transfer of single droplet/wet particle drying. *Chem Eng Sci*. 2008;63:12–23.
11. Handscomb C, Kraft M, Bayly A. A new model for the drying of droplets containing suspended solids. *Chem Eng Sci*. 2009;64:628–637.
12. Handscomb C, Kraft M, Bayly A. A new model for the drying of droplets containing suspended solids after shell formation. *Chem Eng Sci*. 2009;64:228–246.
13. Gharagozloo P, Goodson K. Temperature-dependent aggregation and diffusion in nanofluids. *Int J Heat Mass Transfer*. 2011;54:797–806.
14. Renksizbulut M, Yuen M. Experimental study of droplet evaporation with variable properties and internal circulation at intermediate Reynolds numbers. *Int J Multiphase Flow*. 1983;14:189–202.

15. Grigoriev V, Zorin V. *Thermal Engineering Handbook*, Vol. 1. Moscow: Energoatomizdat (in Russian), 1988.
16. Crank J. *Free and Moving Boundary Problems*. Oxford: Clarendon Press, 1996.
17. Kumar J, Peglow M, Warnecke G, Heinrich S. An efficient numerical technique for solving population balance equations involving aggregation, breakage, growth and nucleation. *Powder Technol*. 2008;182:81–104.
18. Shampine L, Reichelt M. The MATLAB ODE Suite. *SIAM J Sci Comput*. 1997;18:1–22.
19. Tourbin M, Frances C. Experimental characterization and population balance modelling of the dense silica suspensions aggregation process. *Chem Eng Sci*. 2008;63:5239–5351.

Manuscript received July 13, 2011, and revision received Nov. 21, 2011.